nature communications

Article

https://doi.org/10.1038/s41467-025-64180-w

Sub-10 nm upconversion nanocrystals for long-term single-particle tracking

Received: 22 October 2024

Accepted: 8 September 2025

Published online: 24 October 2025

Check for updates

Xiaochen Qiu[1,2,5], Daoming Guan[1,5], Xiaojing Xia[3,5], Huan Ling[1], Jialing Hu[1], Yunxiang Zhang[1] ✉, Emory Chan[3] ✉, Fuyou Li[4] ✉ & Qian Liu[1] ✉

Lanthanide-doped upconversion nanoparticles are attractive single-molecule imaging probes due to their high photostability and anti-Stokes luminescence. However, achieving both small particle size and strong brightness has remained a major challenge, as reducing size often leads to dimmer emission. Herein, we fabricate a sub-10 nm cascade actively protected upconversion nanoparticles, which shows a 33-fold enhanced upconversion efficiency at the single-particle level compared to larger ~19 nm conventional nanoparticles. Theoretical modeling and time-resolved measurements show that emission loss mainly comes from energy leakage of Er^{3+} ions to surface defects. By introducing a $NaYbF_4$ layer as photon-harvesting and protective intermediate layer, we minimize this energy loss and significantly boost brightness. A monolayer of inert $NaLuF_4$ can effectively suppress the surface quenching to Yb^{3+}. Using these ultra-small bright probes, we successfully tracked single epidermal growth factor receptor molecules on live cells for up to one hour, revealing dynamic switching between different diffusion modes.

In the last three decades, optical microscopy has been transformed through the observation of single-molecules[1–5]. Single-molecule tracking has become a powerful tool for studying dynamic molecular interactions in a range of fields, including live cells and novel catalytic supports, because this technique can reveal dynamics in the structure-function relationships underlying the complexity of such systems[6,7]. Single-molecule tracking relies heavily on labeling probes, such as the well-known fluorescent proteins and small organic dyes[8]. However, these labeling probes are limited by their poor photostability and photo-blinking[9]. Typically, the fluorescence only persists for several seconds to one minute, even with the help of a proper oxygen scavenging system[10–12] or triplet quenchers[13–16]. Compared to organic probes, inorganic analogues are generally more thermal- and photo-stable[17,18].

In particular, lanthanide-doped upconversion nanoparticles (UCNPs) show attractive optical properties, such as the lack of photobleaching under single-molecule imaging conditions[19–24]. In such materials, the absorption and emission are insensitive to the environment around the particles due to the inner shell transitions between *4f* electronic states[25]. In addition, using upconversion luminescence (UCL) as an anti-Stokes signal can eliminate interference from auto-fluorescence and achieve background free imaging of biological samples[26–28]. Chu et al., Przybilla et al. and our group have demonstrated the potential of UCNPs for long-term, high-resolution tracking of biomolecules within live-cell environments, highlighting their unique advantages, such as photostability, minimal background noise, and the absence of photoblinking[29–31]. However, the particle sizes in these reports remain larger, which poses challenges for intracellular applications that require minimal steric hindrance.

Unfortunately, UCNPs suffer from the tradeoff between brightness and size. Smaller nanoparticles, especially those with dimensions comparable to fluorescent proteins (<10 nm), exhibit

[1]Department of Chemistry and Shanghai Key Laboratory of Molecular Catalysis and Innovative Materials, Fudan University, Shanghai, PR China. [2]State Key Laboratory of Radio Frequency Heterogeneous Integration, College of Electronics and Information Engineering, Shenzhen University, Shenzhen, PR China. [3]The Molecular Foundry, Lawrence Berkeley National Laboratory, Berkeley, CA, USA. [4]School of Chemistry and Chemical Engineering &Institute of Translational Medicine, Shanghai Jiao Tong University, Shanghai, PR China. [5]These authors contributed equally: Xiaochen Qiu, Daoming Guan, Xiaojing Xia. ✉e-mail: zyx@fudan.edu.cn; EMChan@lbl.gov; lifuyou@sjtu.edu.cn; qianliu@fudan.edu.cn

disproportionately lower intensities and upconversion efficiencies at the single-particle level due to increased surface quenching and smaller numbers of active ions[32,33]. Passivation of UCNPs with inert shells can suppress surface quenching and enhance brightness, but at the expense of larger particle sizes. Organic ligand sensitization strategies have been developed to enhance UCL emission by improving photon harvesting capabilities or energy transfer efficiencies[34] but are undercut by the weak thermal- and photo-stability of the organic ligands. Therefore, it remains a critical challenge to engineer ultrasmall UCNPs with high brightness and photostability for single-particle tracking[35].

The quenching of UCL is challenging to mitigate because its pathways are deeply intertwined with the complex network of photophysical interactions between the numerous excited states of each lanthanide dopant (e.g., energy migration, cross-relaxation and deleterious vibrational relaxation) that give rise to upconversion[36]. In this work, we systematically investigated the surface quenching effects of Yb^{3+} and Er^{3+} in ultrasmall UCNPs using core–shell $NaYbF_4$ and $NaErF_4$ nanocrystals with $NaLuF_4$ inert shells. We synthesized a library of nanoparticles with controlled shell thicknesses (0–4 nm) and evaluated their luminescence properties using both experiments and kinetic Monte Carlo simulations. We show that Er^{3+} ions couple an order of magnitude more strongly to surface quenching sites than Yb^{3+} ions, requiring thicker inert shells to achieve comparable levels of passivation. These insights provide design principles for engineering ultrasmall UCNPs with enhanced brightness and photostability, thereby facilitating their use in single-molecule tracking and in vivo imaging applications.

Results

In order to understand the energy loss mechanisms related to surface and obtain ultrasmall and super-bright UCNPs, we investigated the surface quenching effect on both Yb^{3+} and Er^{3+} in nanocrystals (Fig. 1), respectively. Yb^{3+} ions have a longer excited-state lifetime (~2 ms) compared to Er^{3+} (~400 μs), which intuitively suggests a higher probability of energy loss to surface quenchers for Yb^{3+}. However, Er^{3+} possesses a richer energy-level structure and participates in multiple upconversion processes (e.g., $^2H_{11/2}$, $^4S_{3/2} \rightarrow {}^4I_{15/2}$ and $^4F_{9/2} \rightarrow {}^4I_{15/2}$), making the actual surface quenching behavior more complex and not trivially predictable. We synthesized a series of $NaErF_4$ or $NaYbF_4$ nanoparticles protected with inert outer shells. Due to the minimized lattice mismatch between $NaLuF_4$ and $NaYbF_4$ or $NaErF_4$, we chose $NaLuF_4$ as the substrate material for the shells. All nanoparticles were prepared by a modified solvothermal method[37] and dispersed in the cyclohexane solution (details shown in SI). The diameters of both sets of cores were approximately 11.5 nm and $NaLuF_4$ shells of different thicknesses were coated with thicknesses ranging from 0 to 4 nm (Fig. 1a, Supplementary Figs. S1 and S2). As shown in Fig. 1b, c, the luminescence lifetimes of both Er^{3+} ($^4F_{9/2}$, 654 nm) and Yb^{3+} ($^2F_{5/2}$, 980 nm) were elongated as the $NaLuF_4$ shell thickness increased. After coating with a 4-nm $NaLuF_4$ shell, the lifetime of Er^{3+} increased to 65.9 μs from 1.9 μs. However, it is still significantly shorter than the 470 μs intrinsic lifetime of Er^{3+} (Fig. 1d), which is the luminescence lifetime in the absence of non-radiative decay, indicating a 100% quantum yield. In contrast, the lifetime of Yb^{3+} was increased to 930.7 μs by inert-shell protection, which is 41% of its intrinsic lifetime (2300 μs for Yb^{3+}, Fig. 1e). We then plotted the dependence of the quantum yield (defined as the measured lifetime/intrinsic lifetime) on the inert-shell thickness (Supplementary Fig. S3). For $NaYbF_4$, 1.8 nm inert-shell passivation produced the maximum quantum yield enhancement; while for $NaErF_4$, a thicker than 4.1 nm inert shell is favorable for suppressing surface quenching. These results indicate that, compared to $NaYbF_4$, $NaErF_4$ suffers more severe surface quenching, thus requiring the protection of thicker shells. These results are supported by kinetic Monte Carlo simulations[36,38] of $NaYbF_4$ and $NaErF_4$ nanocrystals that account for energy transfer interactions between each lanthanide ion and the surface (Fig. 1f, g, see SI for simulation details). Simulated lifetimes and intensities exhibit the closest agreement with experiment (e.g., Figs. 1 and 4, Supplementary Fig. S4) when theoretical surface quenching sites are tuned to couple 10-fold more strongly to Er^{3+} than Yb^{3+} (Table S2, Table S3, and Table S4). Alternate schemes, e.g., in which the two dopants couple equally strongly to the surface, fail to qualitatively reproduce experimental trends across the different heterostructures and excitation powers shown in Fig. 4c. The 10-fold stronger coupling of Er^{3+} to surface sites results in interactions between Yb^{3+} ions and the surface decreasing substantially faster than that between Er^{3+} and surface interactions (Supplementary Table S5). By increasing the inert shell thickness from 0 to 1.8 nm, the total energy transfer rate (s^{-1}) between Yb^{3+} and surface species decreases to 0.01% of the rate without an inert shell (Supplementary Table S6), while it drops to 3.68% for Er^{3+}, further supporting our conclusion that Er^{3+} ions need a larger inert shell to achieve the same level of passivation.

In light of the higher sensitivity of Er^{3+} to surface quenching, we hypothesized that a $NaYbF_4$ intermediate layer strategy could enhance UCL emission in a volume-constrained nanoparticle (Fig. 2a). The $NaYbF_4$ layer would not only increase the absorption of excitation photons, but also serve as a spacer between Er^{3+} and the surface, thereby reducing surface quenching of Er^{3+}. To verify our hypothesis, we synthesized a series of core-shell-shell upconversion nanoparticles with 1.5 nm-thick intermediate shells of various compositions, including pure sensitizer $NaYbF_4$, $NaYbF_4$ doped with Er^{3+} (sensitizer mixed with emitter), and inert $NaLuF_4$. For all nanoparticles, $NaYbF_4$:8%Er cores were used to produce bright upconversion signal for single-particle imaging.

It is worth noting that Lu^{3+} exhibits superior lattice compatibility with Yb^{3+} compared to Y^{3+}. The minimal lattice mismatch with the slightly smaller ionic radius of the Lu^{3+} ions leads to the formation of a compressive shell, which facilitates coherent epitaxial growth. This structural advantage effectively suppresses interfacial defects, thereby enhancing upconversion luminescence[31]. Then, the nanocrystals were encapsulated by an outermost shell of $NaLuF_4$ (~0.5 nm), whose minimal thickness (~1 monolayer) was designed to maximize the number of active ions in a volume-constrained nanoparticle. Transmission electron microscopy (TEM) images reveal $NaYbF_4$:8% Er^{3+} cores with uniform size of 10 ± 0.4 nm (Supplementary Fig. S5a). After coating with a 1.5-nm intermediate layer (Supplementary Fig. S5b, Supplementary Fig. S6a and b) and a 0.5-nm outer $NaLuF_4$ shell, the following core-shell-shell structures with a size of ~14 nm were obtained: $NaYbF_4$:8% Er@$NaYbF_4$@$NaLuF_4$, hereafter referred to as Yb:Er@$Yb^{1.5\,nm}$@$Lu^{0.5\,nm}$ or Cascade Actively Protected UCNPs (capUCNPs: Fig. 2b); $NaYbF_4$:8% Er@$NaYbF_4$:8%Er@$NaLuF_4$ (Yb:Er@Yb:$Er^{1.5\,nm}$@$Lu^{0.5\,nm}$, Supplementary Fig. S6c); and $NaYbF_4$:8%Er@$NaLuF_4$@$NaLuF_4$ (Yb:Er@$Lu^{1.5\,nm}$@$Lu^{0.5\,nm}$, Supplementary Fig. S6d). Powder X-ray diffraction (XRD, Supplementary Fig. S7a) and high-resolution TEM (Supplementary Fig. S5c) show the hexagonal phase of the as-synthesized core-shell-shell nanoparticles, which is consistent with the electron diffraction pattern (Supplementary Fig. S7b).

The ensemble upconversion luminescence (UCL) spectra under 980 nm laser excitation display emission peaks at 542 nm (Er^{3+}:$^4S_{3/2} \rightarrow {}^4I_{15/2}$) and 654 nm ($Er^{3+}$:$^4F_{9/2} \rightarrow {}^4I_{15/2}$) (Fig. 2c). Both Yb:Er@Yb:$Er^{1.5\,nm}$ and Yb:Er@Yb:$Er^{1.5\,nm}$@$Lu^{0.5\,nm}$ exhibited very dim UCL emissions, which indicate that the thin, 0.5-nm thick $NaLuF_4$ shell cannot suppress the surface quenching on $NaYbF_4$:8%Er effectively. Similar to previous reports, a thicker, 1.5 nm inert $NaLuF_4$ shell (Yb:Er@$Lu^{1.5\,nm}$) produced significant enhancement on the $NaYbF_4$:8%Er core UCL emission, and the addition of a 0.5-nm $NaLuF_4$ outer shell (Yb:Er@$Lu^{1.5\,nm}$@ $Lu^{0.5\,nm}$) resulted in even greater improvement. Surprisingly, compared to the 10-nm $NaYbF_4$:8%Er core nanoparticles, an intermediate shell of $NaYbF_4$ (Yb:Er@$Yb^{1.5\,nm}$) produced a 2259-fold enhancement in the

https://doi.org/10.1038/s41467-025-64180-w

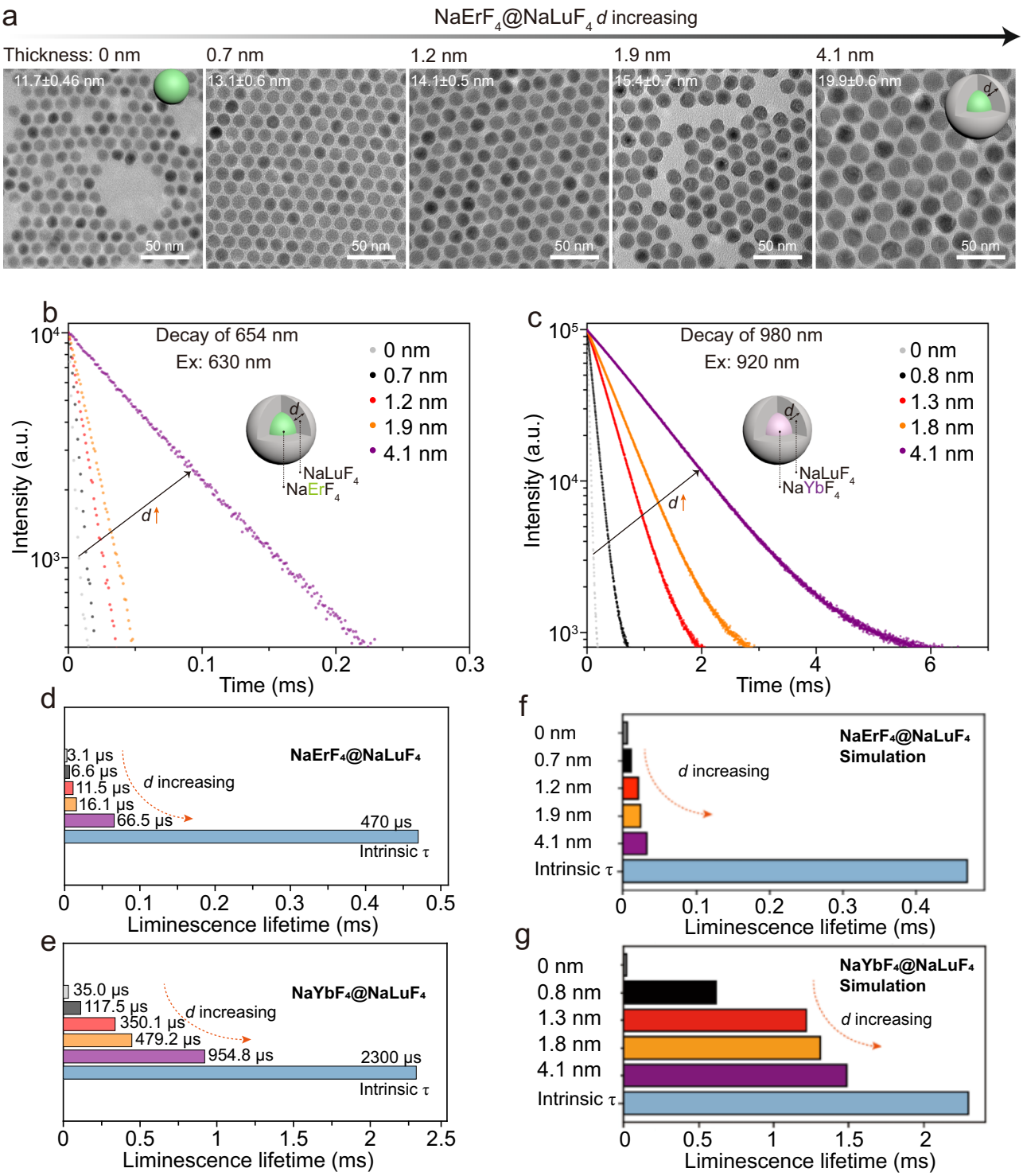

Fig. 1 | Surface quenching tuning of $NaErF_4$ and $NaYbF_4$ via inert $NaLuF_4$ shells. **a** TEM images of $NaErF_4$@$NaLuF_4$ core-shell structure overcoated with various thickness $NaLuF_4$, scale bar: 50 nm. Luminescence decay curves and corresponding calculated luminescence lifetime of (**b**, **d**) $NaErF_4$ and (**c**, **e**) $NaYbF_4$ coated by $NaLuF_4$ with various thickness. The emission of Er^{3+} and Yb^{3+} is collected at 654 and 980 nm under the excitation at 630 and 920 nm, respectively. The luminescence lifetime was fitted according to a single exponential decay function. **f**, **g** fitted lifetimes from kinetic Monte Carlo lifetime traces corresponds to (**d**, **e**). The nanoparticles were stabilized with oleic acid (OA) ligands and dispersed in cyclohexane solution. "a. u." represents "arbitrary units".

UCL, even without an inert shell. The UCL intensity was further enhanced 39-fold by growing a 0.5 nm $NaLuF_4$ shell (capUCNPs: Yb:Er@$Yb^{1.5\,nm}$@$Lu^{0.5\,nm}$), which was close to that of Yb:Er@$Lu^{1.5\,nm}$@$Lu^{0.5\,nm}$. UCL lifetimes of Er^{3+} results showed that the coated $NaYbF_4$ shell (Yb:Er@$Yb^{1.5\,nm}$, 34.4 μs) significantly prolonged the UCL lifetime of the core $NaYbF_4$:8%Er (17.9 μs), indicating that the $NaYbF_4$ layer could reduce surface quenching of excited Er^{3+} ions. Moreover, with additional coating of the 0.5-nm $NaLuF_4$ layer, the luminescence lifetime was further lengthened to 79.0 μs, comparable with that of Yb:Er@$Lu^{1.5\,nm}$@$Lu^{0.5\,nm}$ (79.6 μs). In contrast, incorporating even a small amount of Er^{3+} (8%) in the intermediate $NaYbF_4$ layer (Yb:Er@Yb:$Er^{1.5\,nm}$@$Lu^{0.5\,nm}$) induced a significant reduction in UCL

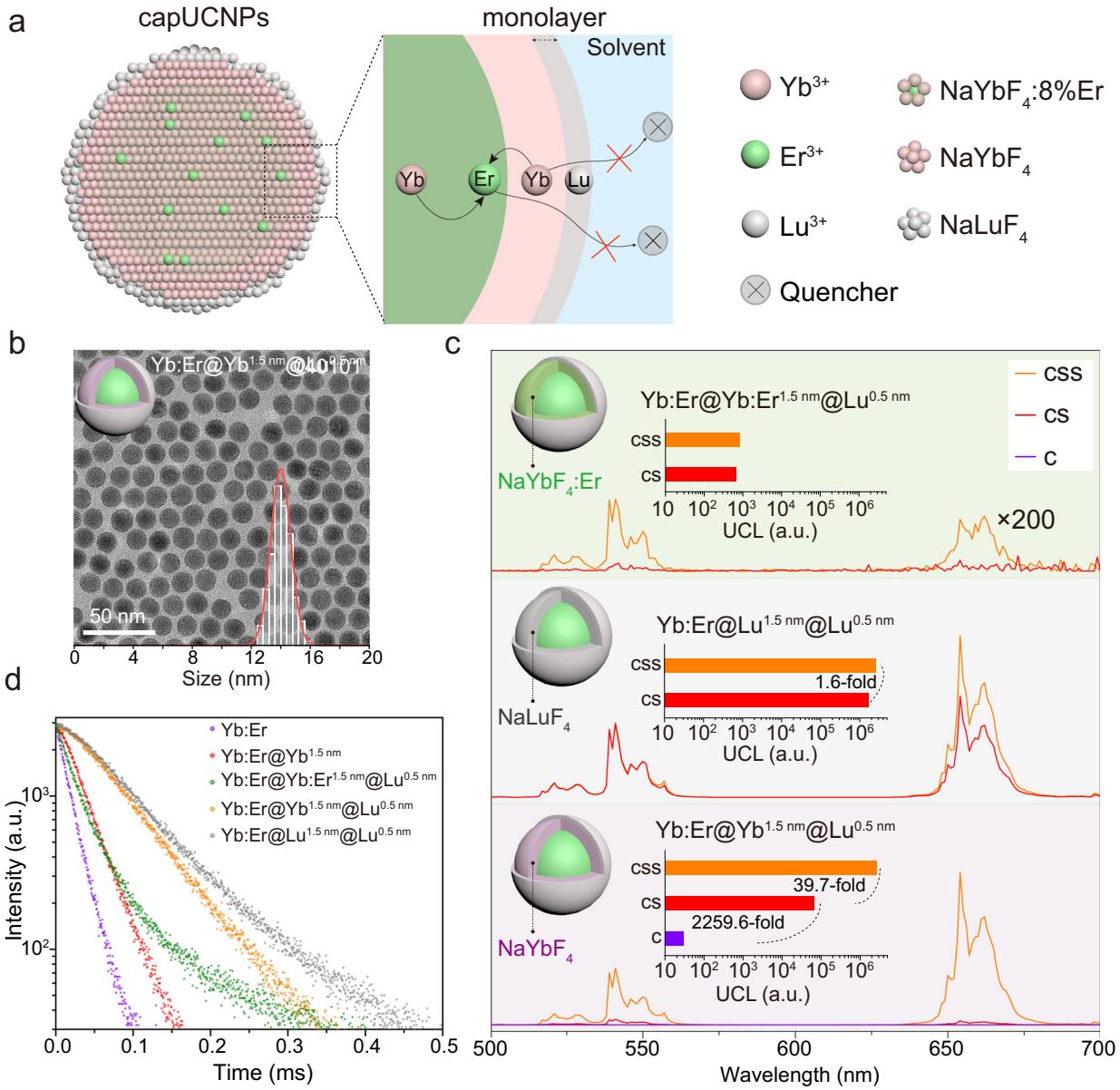

Fig. 2 | Characterization of ~ 14 nm core-shell-shell UCNPs. a Schematic illustration of high brightness capUCNPs *via* a sandwiched structure with $NaYbF_4$ as intermediate layer. **b** TEM images of capUCNPs of Yb:Er@$Yb^{1.5\,nm}$@$Lu^{0.5\,nm}$. **c** Upconversion emission spectra of the as-prepared capUCNPs, Yb:Er@$Lu^{1.5\,nm}$@$Lu^{0.5\,nm}$ and Yb:Er@Yb:$Er^{1.5\,nm}$@$Lu^{0.5\,nm}$ nanoparticle and their corresponding core-shell and core nanoparticles. All spectra were recorded under excitation of a 980 nm CW diode laser at a power density of 530 W cm^{-2}; **d** Upconversion luminescence decay curves of Er^{3+} emission at 654 nm for Yb: Er, Yb: Er@Yb and various sandwich structured nanoparticles with $NaLuF_4$ coating. The nanoparticles were stabilized with oleic acid (OA) ligands and dispersed in cyclohexane solution. "a. u." represents "arbitrary units".

lifetime (16.8 μs) compared to that of pure $NaYbF_4$ layer (Yb:Er@$Yb^{1.5\,nm}$@$Lu^{0.5\,nm}$, 79.0 μs), suggesting that Er^{3+} is primarily responsible for leaking energy to the surface quencher (Fig. 2d). In brief, spectral and lifetime results support our hypothesis that $NaYbF_4$ shells can protect core Er^{3+} ions from surface quenching, and that Yb^{3+} is not as sensitive as Er^{3+} to surface quenching. A thin inert shell of $NaLuF_4$ is all that is necessary to minimize surface effects.

The above ensemble measurements demonstrate that the capUCNPs, with $NaYbF_4$ as an intermediate shell, has similar UCL intensity and lifetime to that of UCNPs with well-protected thicker inert-shells, i.e., Yb:Er@$Lu^{1.5\,nm}$@$Lu^{0.5\,nm}$. However, the ensemble measurement was carried out under a relatively low irradiance. We speculated that the capUCNPs should have better performance than that of Yb:Er@$Lu^{1.5\,nm}$@$Lu^{0.5\,nm}$ under single molecule imaging conditions with higher irradiance, given that the former contains more Yb^{3+} sensitizer and has enhanced light harvesting capability. In order to obtain optimal single-particle brightness, we also adjusted the thickness of the intermediate shell from 1.5 nm to 1.0 nm and the outmost shell from 0.5 nm to 1.0 nm (Supplementary Fig. S8), while keeping the core and overall size unchanged. Two additional core-shell-shell nanoparticles were synthesized, denoted as Yb:Er@$Yb^{1.0\,nm}$@$Lu^{1.0\,nm}$ and Yb:Er@Yb:$Er^{1.0\,nm}$@$Lu^{1.0\,nm}$. We characterized the ensemble optical properties of these particles, and similar results to the Yb:Er@$Yb^{1.5\,nm}$@$Lu^{0.5\,nm}$ series were observed (Supplementary Figs. S9–12). Yb:Er@$Yb^{1.0\,nm}$@$Lu^{1.0\,nm}$ showed much stronger UCL emission than that of Yb:Er@Yb:$Er^{1.0\,nm}$@$Lu^{1.0\,nm}$.

Subsequently, we quantified the brightness of single particles of these UCNPs compositions (Fig. 3) with a home-built wide-field microscope system. After correcting the wide-field luminescence images by the laser illumination profile according to our previous

https://doi.org/10.1038/s41467-025-64180-w

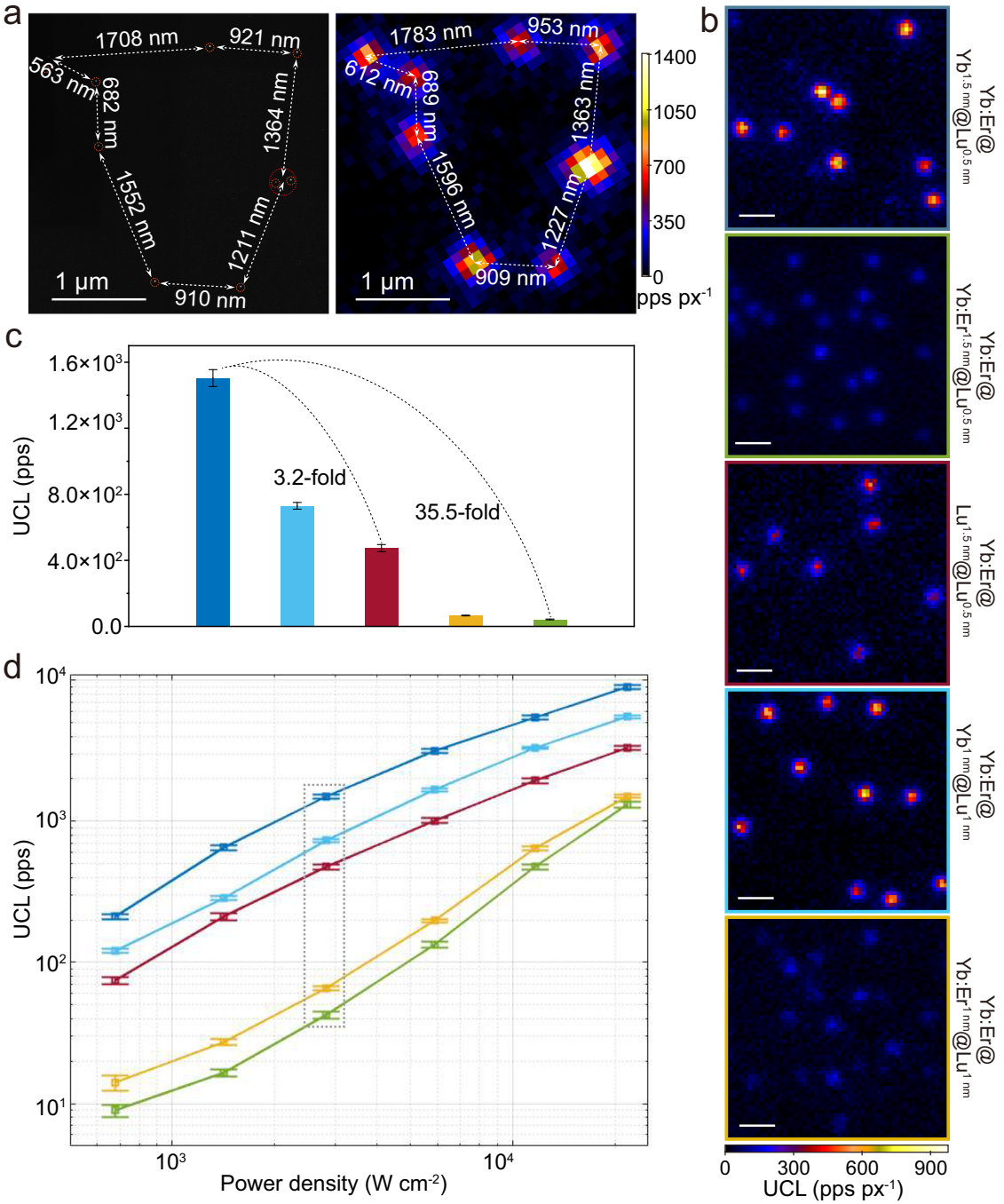

Fig. 3 | Single-particle characterization of ~ 14 nm core-shell-shell UCNPs. a SEM images and corresponding wide-field UCL images of capUCNPs measured at 21.7 kW cm^{-2}. Scale bars, 1 μm; **b** Wide-field UCL images of various ~14 nm sandwich structured nanoparticles measured at 21.7 kW cm^{-2}. Scale bars, 1 μm; **c** The average UCL intensities at 2.8 kW cm^{-2}. The results were presented as means ± standard deviation, three independent experiments, more than five FOVs were acquired for each experiments, $n = 200$. **d** UCL intensity curves at power densities from 680 W cm^{-2} to 21.7 kW cm^{-2} obtained with wide-field microscope. pps: photons per second, pps px^{-1}: photons per second per pixel (blue: capUCNPs-Yb:Er@$Yb^{1.5\,nm}$@$Lu^{0.5\,nm}$, green: Yb:Er@Yb:$Er^{1.5\,nm}$@$Lu^{0.5\,nm}$, red: Yb:Er@$Lu^{1.5\,nm}$@$Lu^{0.5\,nm}$, light blue: Yb:Er@$Yb^{1\,nm}$@$Lu^{1\,nm}$ and yellow: Yb:Er@Yb:$Er^{1\,nm}$@$Lu^{1\,nm}$). The nanoparticles were stabilized with OA ligands and immobilized on a cover glass substrate. The results were presented as means ± standard deviation, three independent experiments, more than five FOVs were acquired for each experiments, $n = 200$.

report[19], the diffraction-limited luminescence spots were carefully registered to corresponding positions on electron micrographs (Fig. 3a) and single-particle upconversion emission was demonstrated. We first measured all five types of UCNPs at 2.8 kW cm^{-2}, a moderate power density for single molecule imaging. capUCNPs Yb:Er@$Yb^{1.5\,nm}$@$Lu^{0.5\,nm}$ emits approximately 1500 photons per second (pps, obtained from the integrated volume of the two-dimensional Gaussian fit), 35.5 times brighter than Yb:Er@Yb:$Er^{1.5\,nm}$@$Lu^{0.5\,nm}$ (Fig. 3c), which was consistent with the ensemble spectra and lifetime results and indicated Er^{3+} as the main species being quenched by the surface. Compared to Yb:Er@$Yb^{1.0\,nm}$@$Lu^{1.0\,nm}$, Yb:Er@$Yb^{1.5\,nm}$@$Lu^{0.5\,nm}$ also exhibited enhanced UCL emission, suggesting that the quantity of Yb^{3+} sensitizer is critical for single-particle imaging while a thicker inert shell is unnecessary in the volume-constrained nanoparticles under

single molecule imaging condition. To further investigate the power-dependent behavior of single-particle luminescence, measurements on hundreds of individual nanoparticles at power densities from 680 W cm^{-2} to 21.7 kW cm^{-2} were used to plot saturation curves (Fig. 3d). capUCNPs Yb:Er@Yb$^{1.5\,nm}$@Lu$^{0.5\,nm}$ showed brighter emission over other UCNPs at all power densities investigated. Yb:Er@Yb:Er$^{1.5\,nm}$@Lu$^{0.5\,nm}$ and Yb:Er@Yb:Er$^{1\ nm}$@Lu$^{1\,nm}$ saturation curves exhibited steeper slopes, indicating the existence of severe energy quenching in both types of UCNPs.

In order to determine whether the enhanced UCL emission results from the specific core-shell-shell arrangement or only from the enriched sensitizer Yb^{3+}, we mixed the intermediate $NaYbF_4$ layer with the outmost $NaLuF_4$ layer and synthesized a series of core-shell nanoparticles with an overall size of about 14 nm (Supplementary Figs. S14a and S13); 10 nm $NaYbF_4$:8%Er nanoparticles were still used as the core, and the outmost layer is 2 nm $NaLuF_4$ shell with different ratios of Yb^{3+} doping. Ensemble measurements (Supplementary Fig. S15a) reveal that core-shell UCNPs become dimmer as Yb^{3+} doping concentration increases. And the UCL lifetimes were shortened as Yb^{3+} doping concentration in shell increased (Supplementary Figs. S15b and S15c). Single-particle measurements also demonstrated that Yb^{3+} doping in the shell causes a significant decrease in UCL brightness (Supplementary Fig. S14b, c and Fig. S16), even at the highest irradiance of 21.7 kW cm^{-2}. The above results demonstrated the significance of core-shell-shell structure with separated $NaYbF_4$ and $NaLuF_4$ layers for obtaining stronger UCL emission in smaller volume-constrained nanoparticles.

Seeking to access smaller nanoparticle probes that have minimal influence on labeling targets, we applied this sandwiched design to sub-10 nm UCNPs. In order to obtain ultrasmall and uniform core nanoparticles (6.9 ± 0.5 nm, Supplementary Fig. S17a), we doped a small fraction of Gd^{3+} (~10%) in the $NaYbF_4$:8%Er nanoparticles[39]. Subsequently, the core was coated with a 1.0 nm $NaYbF_4$ intermediate shell (Supplementary Fig. S17) and a 0.5 nm $NaLuF_4$ outmost shell, producing core-shell-shell sandwich UCNPs with an overall size of 9.9 nm (Fig. 4a inset), referred as Yb:Gd,Er$^{7\,nm}$@Yb$^{1\,nm}$@Lu$^{0.5\,nm}$ or sub-10 nm capUCNPs. UCL spectra data revealed that the 0.5 nm $NaLuF_4$ shell produced an impressive enhancement of 2675-fold on this sub-10 nm UCNPs' emission (Fig. 4a). This could be explained by the fact that surface quenching effect is exacerbated as particle size decreases. Therefore, inert-shell protection, even a monolayer of inert crystal lattice, is critical for smaller nanoparticles. Several other types of UCNPs were synthesized as controls, including the inert-shell well-protected $NaYbF_4$:10%Gd,8%Er (referred to as Yb:Gd,Er$^{7\,nm}$@Lu$^{1.5\,nm}$, an overall size of ~10 nm, Supplementary Figs. S18 and S19), conventional UCNPs (18.9-nm $NaYF_4$:20%Yb, 2%Er, Supplementary Fig. S20), and highly Er^{3+}-doped UCNPs ($NaYF_4$:20%Yb,20%Er@$NaLuF_4$, with a 7.6 nm core and an overall size of 10.2 nm, Supplementary Fig. S21).

In single-particle measurements (Fig. 4b), the sub-10 nm capUCNPs exhibited superior performance to all other UCNPs over power densities from 680 W cm^{-2} to 21.7 kW cm^{-2}. (Fig. 4c, e, Supplementary Fig. S22). When imaged on same glass substrate under low power density (680 W cm^{-2}) excitation, sub-10 nm capUCNPs are clearly visible at 0.033 fps, but the conventional ~19 nm UCNPs are not (Fig. 4e), indicating the great potential of our design in wide-field bioimaging applications. As the excitation power increased, the bigger conventional UCNPs continued to increase in brightness, approaching that of the sandwiched structure we designed (Supplementary Fig. S22).

Typically, the UCL intensity varies non-linearly with the particle volume, considering smaller nanoparticles have a greater proportion of lanthanide ions near their surface and suffer heavily from surface quenching. However, in order to have a fair comparison between different sized UCNPs and quantify the UCL efficiency in terms of volume utilization, we calculated their emitted photons per second per cubic nanometer. As shown in Fig. 4f, the sub-10 nm capUCNPs has 33.2-fold improvement in upconversion efficiency over the 6.8-times bigger conventional UCNP at 2.8 kW cm^{-2}. Compared to the efficient sub-10 nm Er^{3+}-rich UCNPs ($NaYF_4$:20%Yb,20%Er@$NaLuF_4$, 10.2 nm), which are structurally similar to those previously reported in the literature[34], our core–shell–shell design exhibits up to one order of magnitude higher brightness under comparable excitation conditions. In addition, we also demonstrated that the 0.5 nm inert shell is critical for the UCL emission and generated 73.4-fold improvement with respect to Yb:Gd,Er$^{7\,nm}$@Yb$^{1\,nm}$ in upconversion efficiency. We believe that the enhancement will be even more significant at even lower power densities, approaching the ensemble results. However, Yb:Gd,Er$^{7\,nm}$@Yb$^{1\,nm}$ is too dim to detect at power densities below 2.8 kW cm^{-2}.

To quantitatively evaluate the impact of nanoparticle size on lateral mobility prior to cellular imaging, we conducted control experiments on a model supported lipid bilayer (SLB) system. The SLB was functionalized with biotin, and biotin-modified UCNPs were tethered via streptavidin-mediated linkage, ensuring attachment (Supplementary Figs. S23–S25). Single-particle tracking revealed a clear size-dependent effect: nanoparticles with larger diameters exhibited significantly lower diffusion coefficients (Supplementary Fig. S26). This inverse relationship between particle size and lateral diffusion underscores the necessity of synthesizing ultrasmall UCNPs to minimize steric hindrance and preserve native biomolecular dynamics during live-cell imaging. Nonetheless, larger UCNPs, owing to their higher density of sensitizers and emission centers, exhibit stronger single-particle brightness and may offer advantages in systems where steric hindrance is less critical.

To demonstrate the utility of these bright sub-10 nm capUCNPs, we used them to perform long-term membrane protein tracking of epidermal growth factor receptor (EGFR, Supplementary Movie 1). The UCNPs were modified with polyacrylic acid (PAA) and further passivated with poly (ethylene glycol) (abbreviated as capUCNPs-PEG). The monoclonal EGFR antibody (anti-EGFR) was conjugated at the end of PEG (abbreviated as capUCNPs-PEG-antiEGFR). TEM and DLS (dynamic light scattering) analysis demonstrated an excellent monodispersity in aqueous solution (Fig. 5a, Supplementary Fig. S27 and Fig. S28). The average number of capUCNPs-PEG-antiEGFR on each cell was around 5 times greater than that of UCNPs-PEG (as control), suggesting a good targeting specificity of capUCNPs-PEG-antiEGFR and the successful conjugation of the antibody (Fig. 5b and Supplementary Fig. S29). Figure 5c showed the representative moving trajectories of EGFRs labeled with capUCNPs-PEG-antiEGFR on a U2OS cell. We analyzed these trajectories of hundreds of capUCNPs-labeled EGFRs using single-molecule tracking software[40]. Due to the high brightness of our nanoparticles and their inherent high photostability, we were able to obtain an average signal-to-noise ratio of 10 (Supplementary Figs. S30–S31) and a tracking duration up to one hour. The SNR analysis was primarily based on signals from individual particles; however, potential contributions from EGFR dimerization or oligomerization cannot be completely ruled out[41]. We note that the loss of tracking was not caused by photobleaching, but rather by the UCNPs moving out of the focal plane (Supplementary Figs. S32 and S33). The spatial localization precision of the tracking was about 12 nm (Fig. 5d)[42], which was comparable with bright organic dyes. Fitting of mean squared displacement (MSD) traces (details was shown in SI) revealed three different modes of movement for EGFR: suppressed diffusion, free diffusion, and directed diffusion. The number of suppressed diffusion molecules accounts for about 69% of the total, which agreed with the previous reports (Supplementary Table S7)[43]. Facilitated by these ultra-long-term tracking durations, we observed that some EGFRs exhibit free diffusion mode in early stages but suppressed diffusion mode in later stages (Supplementary Fig. S34). We even observed switching between several different diffusion modes (Fig. 5f, g), which is difficult to be visualized with organic dyes or fluorescence proteins due to their

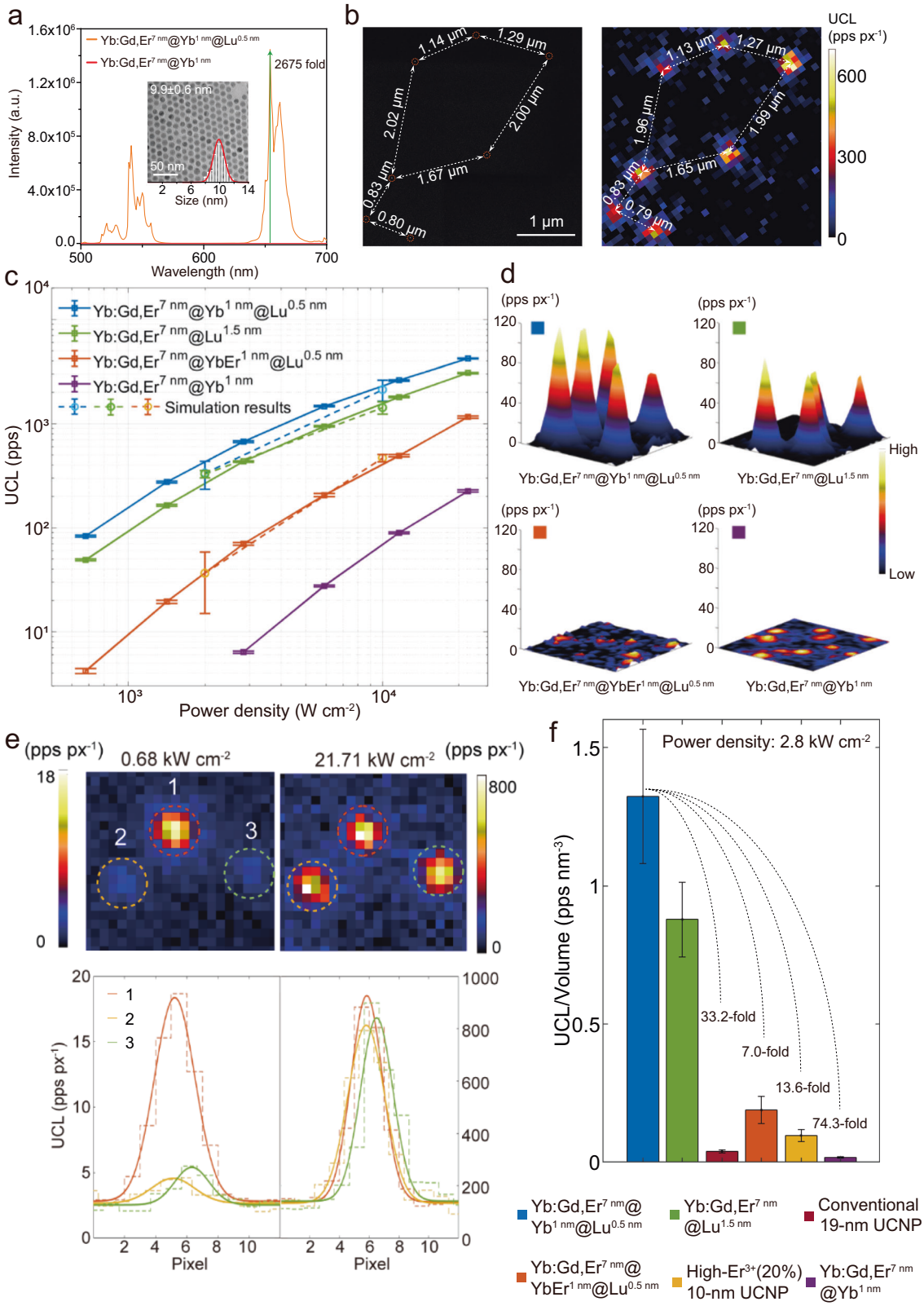

poor photostability. While non-specific adsorption cannot be completely ruled out, its contribution is expected to be minor compared to the antibody-mediated targeting observed (Supplementary Fig. S35). In the future, further development of more refined targeting strategies and optimized surface modification approaches will be crucial for enhancing the specificity of nanoparticle targeting and minimizing non-specific adsorption.

Discussion

We developed a cascade actively protected strategy to enhance the upconversion single-particle brightness in volume-constrained UCNPs by introducing a $NaYbF_4$ intermediate layer. Using kinetic Monte Carlo simulations and lifetime investigations, we demonstrate that Er^{3+} suffers more severe surface quenching than Yb^{3+}. The intermediate layer not only protects Er^{3+} from surface quenching but also increases the

Fig. 4 | Characterization of ultrabright sub-10 nm capUCNPs with a $NaYbF_4$ intermediate layer. a The UCL spectra of $NaYbF_4$:10%Gd,8%Er@$NaYbF_4$@$NaLuF_4$ (referred to as sub-10 nm capUCNPs or Yb:Gd,$Er^{7\,nm}$@$Yb^{1\,nm}$@$Lu^{0.5\,nm}$) and $NaYbF_4$:10%Gd,8%Er@$NaYbF_4$ (referred to as Yb:Gd,$Er^{7\,nm}$@$Yb^{1\,nm}$) under the excitation of 980 nm laser (530 W cm^{-2}). Inset shows TEM image of Yb:Gd,$Er^{7\,nm}$@$Yb^{1\,nm}$@$Lu^{0.5\,nm}$ UCNPs. **b** SEM images and corresponding wide-field UCL image of Yb:Gd,$Er^{7\,nm}$@$Yb^{1\,nm}$@$Lu^{0.5\,nm}$. Scale bars, 1 μm. **c** UCL intensity curves of the nanoparticles at power densities from 680 W cm^{-2} to 21.7 kW cm^{-2} obtained with wide-field microscope. The results were presented as means ± standard deviation, three independent experiments, more than five FOVs were acquired for each experiments, $n = 200$. **d** Three-dimensional representations of the wide-field UCL images at 2.8 kW cm^{-2}, each with a small colored indicator box corresponding to the color scheme shown in (**c**). **e** Wide-field UCL images and corresponding 1D UCL intensity profiles of the mixed particles (particle **1**: sub-10 nm capUCNPs and particle **2** & **3**: conventional 19 nm UCNPs) at power densities of 680 W cm^{-2} and 21.7 kW cm^{-2}. Orange line indicated particle 1, yellow and green line indicated particle 2 and 3, respectively. **f** The per unit volume UCL intensity at 2.8 kW cm^{-2} plotted with a color scheme follows (**c**) and Supplementary Fig. 22. The nanoparticles were stabilized with OA ligands and immobilized on a cover glass substrate. The results were presented as means ± standard deviation, three independent experiments, more than five FOVs were acquired for each experiments, $n = 200$.

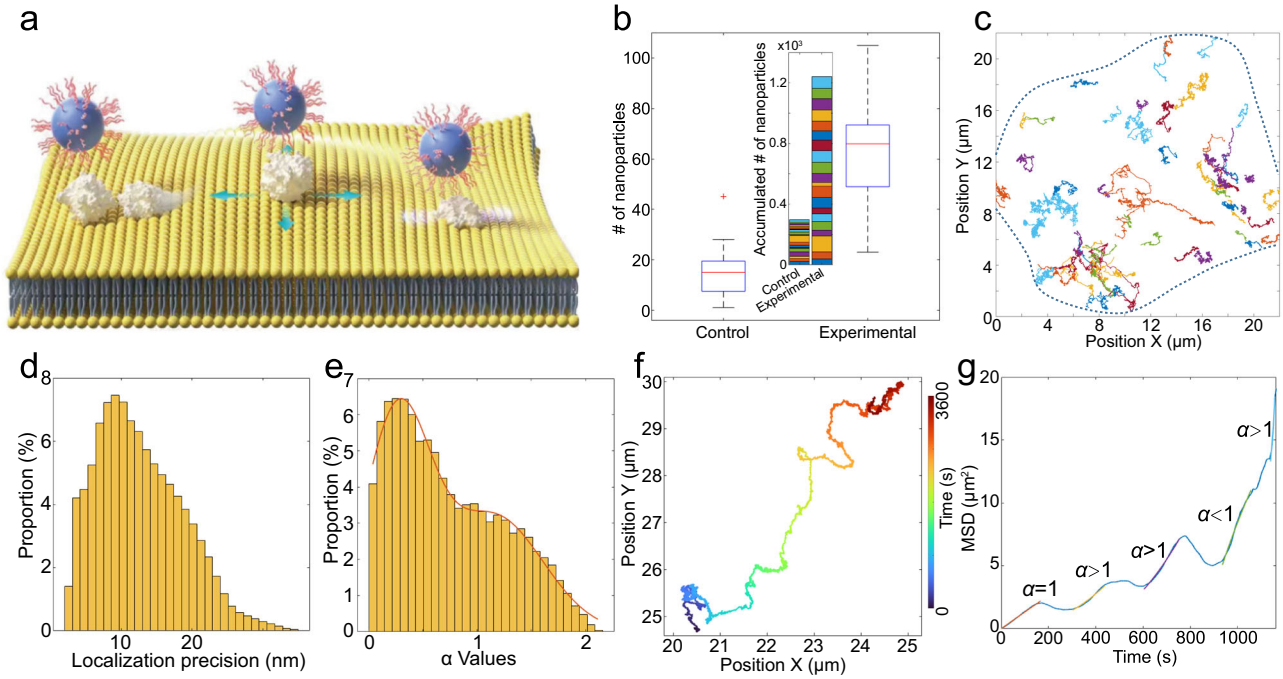

Fig. 5 | Ultra-long-term single-particle tracking of EGFR using sub-10 nm capUCNPs probes. a Schematic diagram illustrating EGFR tracking with anti-EGFR-conjugated sub-10 nm capUCNPs (UCNPs-PEG-antiEGFR). **b** Number of nanoparticles bound to the U2OS cell membrane. UCNPs-PEG was used in the control group, and UCNPs-PEG-antiEGFR was used in the experimental group. The inset shows the accumulation of UCNPs observed in both groups across 20 fields of view (FOVs). The center line indicates the median; box edges denote the 25th and 75th percentiles; whiskers extend to 1.5× the interquartile range; red crosses mark outliers. **c** Movement trajectories of EGFRs labeled with UCNPs-PEG-antiEGFR on a U2OS cell. **d** Distribution of localization precision obtained from Gaussian fitting of point spread functions (PSFs) for capUCNPs conjugated with anti-EGFR antibodies. **e** Distribution of the Alpha (α) values from mean square displacement (MSD) fittings of EGFR trajectories. **f** A representative EGFR trajectory with a temporally encoded color map indicating different timepoints. **g** MSD fittings for the trajectory shown in (**f**), with distinct α values indicating transitions between different diffusion modes for a single capUCNPs-labeled EGFR. The nanoparticles were dispersed in BBS solution for use.

ability of these UCNPs to harvest incident photons. Based on this strategy, we synthesized a sub-10 nm capUCNPs with $NaYbF_4$ as interior shell and a monolayer of $NaLuF_4$ as the outmost shell. Compared to the 19 nm conventional UCNPs, these sub-10 nm sandwich UCNPs shows a 33-fold enhancement in upconversion efficiency at the single-particle level. This is particularly noteworthy, as smaller nanoparticles typically have a larger surface-to-volume ratio, which makes them more susceptible to surface quenching. Furthermore, we employed these super-bright sub-10 nm capUCNPs for single-particle tracking. Thanks to their high brightness and the inherent high photostability, we successfully tracked EGFRs for up to one hour with high localization precision, revealing various diffusion modes of EGFR movements.

Although the long-lived excited states of UCNPs result in lower per-ion emission rate compared to nanosecond-lifetime emitter such as quantum dots, this limitation can be effectively offset by incorporating multiple luminescent centers within each nanoparticle. Looking forward, future efforts may focus on accelerating the excitation-emission cycling process through materials engineering or energy transfer optimization to further boost the upconversion brightness for demanding bioimaging applications. Overall, this work lays the foundation for the development of even smaller and brighter UCNPs, enabling more precise and prolonged single-particle tracking in complex biological environments.

Methods

Synthesis of 10-nm $NaYbF_4$:8%Er core nanoparticles

The 10-nm $NaYbF_4$:8%Er nanoparticles were synthesized according to the previously reported method with some modifications[37]. In a typical experiment, 10.0 mL of oleic acid and 10.0 mL of 1-octadecene was added to a 100-mL three-neck round-bottomed flask following with 1.0-mL aqueous solution of $LnCl_3$ (1 mol/L, Ln = Yb and Er). The water was removed by blowing N_2 at 150 °C for one hour, forming a clear solution. After cooling to room temperature, 2.03 g of NaOA was added to the solution and stirred at 120 °C under vacuum for 30 min. Then 0.34 g ammonia fluoride was added to the mixture and kept at

120 °C for another 30 min. The solution was then heated to 290 °C and maintained at this temperature for 55 min. After cooling to room temperature, the nanoparticles were precipitated by addition of ethanol and dispersed in cyclohexane for further using.

Synthesis of 7-nm $NaYbF_4$:10%Gd,8%Er core nanoparticles

The synthesis of 7-nm $NaYbF_4$:10%Gd,8%Er core nanoparticles were identical to that for 10-nm $NaYbF_4$:8%Er core nanoparticles except for ripening at 300 °C for 30 min.

Synthesis of $NaYbF_4$:10%Gd,8%Er @ $NaYbF_4$ core-shell nanoparticles

The core-shell nanoparticles were prepared via a modified literature procedure[19]. The pre-synthesized core nanoparticles ($NaYbF_4$:8%Er or $NaYbF_4$:10%Gd,8%Er) were used as seeds for shell growing. In a typical experiment, the shell stock aqueous solution was firstly added to a 100 mL three-neck round-bottomed flask containing 3 mL of oleic acid and 8 mL 1-octadecene. The resulting mixture was heated to 150 °C and kept for 30 min to remove the water. Then the solution was cooling down to 50 °C. A cyclohexane dispersion (1 mL) of core nanoparticle seeds was then added along with NH_4F and NaOH. The reaction was stirred under vacuum at 110 °C for 30 min and then heated to 290 °C under a nitrogen atmosphere for 30 min. After cooling to room temperature, the nanoparticles were precipitated by addition of ethanol and dispersed in cyclohexane for further using.

Synthesis of $NaYbF_4$:10%Gd,8%Er @ $NaYbF_4$ @ $NaLuF_4$ core-shell-shell nanoparticles

The synthesis of core-shell-shell nanoparticles was identical to that for core-shell nanoparticles except for the core-shell nanoparticles were used as seeds.

Synthesis of UCNPs@DSPE-PEG-biotin[44]. Redisperse 0.4 mL of the aforementioned UCNPs cyclohexane solution in 2 mL of chloroform and mix it in a 10 mL round-bottom flask with 8 mL of chloroform solution containing 5 mg of DSPE-mPEG (2000 Da) and 0.5 mg of DSPE-mPEG (2000 Da)-biotin. Stir at room temperature for 2 h, then remove the chloroform by rotary evaporation. The resulting film is hydrated with 10 mL of deionized water. Transfer the mixture to a centrifuge tube and remove excess lipids by low-speed centrifugation (112 *g*, 5 min), followed by purification of @DSPE-PEG by ultracentrifugation (25,155 *g*, 15 min). Finally, redisperse @DSPE-PEG in 2 mL of PBS.

Surface modification of capUCNPs for EGFR tracking

For cellular imaging, the capUCNPs were modified with polyacrylic acid (PAA) and further passivated with poly(ethylene glycol), abbreviated as capUCNP-PEG. Typically, 10 mg of PAA (450,000 Da) was added to 10 mL of deionized water, and pH was adjusted to 8 using 0.1 M NaOH under vigorous stirring at room temperature for 30 min. Next, 1 mL capUCNPs was added dropwise to this solution, which was then stirred for an additional 4 h. The resulting mixture was combined with 10 mL of diethylene glycol and heated at 105 °C for 2 h while stirring to facilitate water evaporation. Subsequently, cooling down to the room temperature, the PAA-coated UCNPs, denoted as UCNP-PAA, were collected by centrifugation at 25,155 *g* for 20 min. The UCNP-PAA were washed three times with deionized water and ethanol, redispersed in 1 mL of deionized water (0.25 M), and stored at 4 °C.

To enhance the biocompatibility of the UCNPs, PEG was conjugated to the UCNPs surface. Specifically, 1 mg of UCNP-PAA was added into borate-buffered saline (BBS) buffer (2.5 mM H_3BO_3, 7.5 mM $Na_2B_4O_7$, pH ≈ 8.0), followed by the addition of 100 μg of freshly prepared EDC and 100 μg of Sulfo-NHS. The mixture was stirred for 1 h at room temperature. Afterward, 50 μg of NH_2-PEG_{3800}-COOH was introduced, and the mixture was stirred for an additional 4 h. The capUCNP-PEG were then collected by centrifugation, re-dispersed in BBS buffer, and stored at 4 °C.

Finally, the EGFR antibodies (anti-EGFR, 30H45L8, ABfinity™ Rabbit Monoclonal, ThermoFisher) were conjugated to the terminal PEG groups. In detail, capUCNP-PEG was added into BBS buffer, followed by the addition of 100 μg of freshly prepared EDC and 100 μg of Sulfo-NHS. The mixture was stirred for 1 h at room temperature. Afterward, 10 μg of anti-EGFR was introduced, and the mixture was stirred for an additional 4 h. The capUCNP-PEG-antiEGFR were then collected by centrifugation, re-dispersed in BBS buffer, and stored at 4 °C.

Kinetic Monte Carlo simulations

We used a kinetic Monte Carlo (KMC) model initially developed in ref. 36. to simulate the upconversion luminescence lifetime. This KMC method was adapted for high performance computing[45], with the NPMC source code available within the open source RNMC package[46]. New simulation parameters for Er^{3+} were adapted, and changes are tabulated in Supplementary Table S2. A spherical UCNP was implemented using the rejection-free, Gillespie stochastic simulation algorithm, and the transition probabilities of each KMC step were calculated a previous method used for differential rate equation models[36]. For a given UCNP configuration, the excited state of each individual lanthanide ion was simulated under a given excitation wavelength and power. After a given time, the excitation was discontinued. The KMC lifetime simulations were obtained by monitoring the population changes of certain excited states after the excitation radiation was discontinued. The upconversion luminescence intensity was calculated by averaging the photon emission rate of specified radiative relaxation across the UCNP after reaching the steady state.

Sample preparation for optical characterization

To prepare the sample for wide field imaging, the nanoparticles cyclohexane solution was dropped onto a clean and dry № 1.5 cover glass briefly pre-treated with 1% (w/v) poly-lysine. Before attaching the glass onto a standard microscope, the excess nanoparticles were rinsed off with cyclohexane for several times.

Single-particle imaging in aqueous solution was performed using glass coverslips functionalized with PEG–biotin. UCNPs–PEG–biotin was immobilized on the surface via specific biotin–streptavidin interactions. A solution of 0.5 μg/mL UCNPs–PEG–biotin was injected into the imaging channel, allowing for surface binding. Prior to mounting the coverslip on the microscope, excess unbound nanoparticles were thoroughly rinsed away with PBS to ensure sparse distribution suitable for single-particle analysis.

Wide field imaging

Each kind of UCNP is prepared into single-particle sample in advance and observed under a self-built wide field microscope system equipped with a 100× objective (NA 1.49, Nikon). A laser emitter (BL976-PAG900, Thorlabs) is coupled to the optical path and excites the sample through the objective. The emission from single UCNPs passes through the same objective and is received by an EMCCD (iXon Ultra 897, Andor) coupled to the microscope. An emission filter (ET750sp-2p8, Chroma) is used to filter the emitted light so that almost all of the photons received by the EMCCD comes from the sample. Samples were tested at a range of power densities from 0.68 kW cm^{-2} to 22 kW cm^{-2} to ensure consistency of data at different power density levels.

Single-particle tracking of EGFR using sub-10 nm capUCNP probes. U2OS osteosarcoma cells were obtained from the Institute of Biochemistry and Cell Biology, SIBS, CAS (China, TCHu88, Female). These cell lines are not listed in the database of misidentified cell lines maintained by the International Cell Line Authentication Committee

(ICLAC). Cells were cultured in RPMI 1640 medium supplemented with 10% fetal bovine serum (FBS) at 37 °C in a 5% CO_2 atmosphere. For imaging, cells (20 µL, approximately $5 \times 10^8 L^{-1}$) were seeded onto 14-mm glass coverslips and allowed to adhere for 24 h under 100% humidity.

Prior to labeling, cells were washed with PBS and then incubated in serum-free medium containing 50 µg/mL capUCNP–PEG–anti-EGFR or capUCNP–PEG for 5 minutes at 37 °C under 5% CO_2. After labeling, cells were washed three times with PBS to remove unbound nanoparticles.

Single-particle imaging was performed using a custom-built wide-field fluorescence microscope equipped with a 100× oil-immersion objective (NA 1.49, Nikon). A 976-nm laser diode (BL976-PAG900, Thorlabs) was used for excitation through the objective lens. Emission from individual UCNPs was collected by the same objective, passed through an emission filter (ET750sp-2p8, Chroma) to block scattered excitation light, and detected by an EMCCD camera (iXon Ultra 897, Andor). UCNP tracking was conducted at the apical (top) surface of the cells. For the live-cell experiments, a continuous-wave 976 nm laser was used with an excitation power density of 16.6 kW/cm². Luminescence images were acquired with an exposure time of 150 ms per frame at a frame rate of approximately 6.7 frames per second. Imaging was performed continuously for 1 h to monitor long-term particle dynamics under physiological conditions. Significantly brighter events as those with intensity exceeding the mean + 2σ was excluded in the data analysis. Hundreds of trajectories of capUCNPs-labeled EGFRs were analyzed.

We also performed a blocking experiment in which U2OS cells were pre-incubated with free anti-EGFR antibody (10 µg/mL) for 1 h prior to the addition of anti-EGFR functionalized capUCNPs (50 µg/mL). This pre-treatment effectively saturated EGFR on the cell surface, thereby preventing further binding by the nanoparticle-bound antibody.

Evaluation method for single-particle UCL intensity

The point spread function (PSF) of each single UCNP is fitted by the following two-dimensional Gaussian function:

$$I(x,y) = \frac{I_0}{2\pi\sigma_x\sigma_y} exp\left(-\frac{\left(cos(\theta)x + sin(\theta)y - x_0\right)^2}{2\sigma_x^2} - \frac{\left(-sin(\theta)x + cos(\theta)y - y_0\right)^2}{2\sigma_y^2}\right) + C \quad (1)$$

Where θ is tilt angle, x_0 and y_0 are the center position of the PSF, σ_x and σ_y are the standard deviation in x and y directions, I_0 is the total number of photons of the PSF, and C is background. The aggregated particles are not counted by the program. The UCL intensity of each particle is defined as the number of photons emitted per unit time:

$$I_{x_0y_0} = \frac{\iint_{-\infty}^{\infty} \frac{I_0}{2\pi\sigma_x\sigma_y} exp\left(-\frac{\left(cos(\theta)x + sin(\theta)y - x_0\right)^2}{2\sigma_x^2} - \frac{\left(-sin(\theta)x + cos(\theta)y - y_0\right)^2}{2\sigma_y^2}\right)}{\tau} \quad (2)$$

Where τ is exposure time of EMCCD. For each single-particle sample, we counted hundreds of PSFs to ensure the accuracy of the data. The UCL intensity of each UCNP sample is the average of the UCL intensity of single UCNPs included in the statics.

Localization precision. The localization uncertainty was estimated based on a widely accepted theoretical expression for fluorescence spot localization precision[47].

$$\left\langle (\Delta x)^2 \right\rangle = \frac{s^2 + \frac{a^2}{12}}{N} + \frac{8\pi s^4 b^2}{a^2 N^2} \quad (3)$$

Where s is the standard deviation of PSF, a is the camera pixel size, N is the number of photons emitted by the molecule, and b^2 is the variance of the camera background noise per pixel.

MSD fitting

We fitted the mean squared displacement (MSD) of each trajectory of localized molecules with power law:

$$MSD = 4Dt^{\alpha} + offset \quad (4)$$

where D is diffusion constant and α is a coefficient that indicates the motion type. Various movement modes of UCNP-labeled EGFR were observed: suppressed diffusion mode ($\alpha < 1$), free diffusion mode ($\alpha \sim 1$) and directed diffusion ($\alpha > 1$).

Statistics and reproducibility

All single-particle imaging and tracking experiments were repeated independently three times with similar results.

Reporting summary

Further information on research design is available in the Nature Portfolio Reporting Summary linked to this article.

Data availability

All data that support the findings of this study are presented in the manuscript and in the supplementary information file. Source data are provided with this paper. Raw data for this study are available from the authors on request. Source data are provided with this paper.

References

1. Betzig, E. & Chichester, R. J. Single molecules observed by near-field scanning optical microscopy. *Science* **262**, 1422–1425 (1993).
2. Perkins, T. T., Quake, S. R., Smith, D. E. & Chu, S. Relaxation of a single DNA molecule observed by optical microscopy. *Science* **264**, 822–826 (1994).
3. Yildiz, A. et al. Myosin V walks hand-over-hand: single fluorophore imaging with 1.5-nm localization. *Science* **300**, 2061–2065 (2003).
4. Betzig, E. et al. Imaging intracellular fluorescent proteins at nanometer resolution. *Science* **313**, 1642–1645 (2006).
5. Taniguchi, Y. et al. Quantifying E. coli proteome and transcriptome with single-molecule sensitivity in single cells. *Science* **329**, 533–538 (2010).
6. Shen, H. et al. Single particle tracking: from theory to biophysical applications. *Chem. Rev.* **117**, 7331–7376 (2017).
7. Chen, J. et al. Single-molecule dynamics of enhanceosome assembly in embryonic stem cells. *Cell* **156**, 1274–1285 (2014).
8. Mo, G. C. H. et al. Genetically encoded biosensors for visualizing live-cell biochemical activity at super-resolution. *Nat. Methods* **14**, 427–434 (2017).
9. Basu, S. et al. FRET-enhanced photostability allows improved single-molecule tracking of proteins and protein complexes in live mammalian cells. *Nat. Commun.* **9**, 2520 (2018).
10. Rasnik, I., McKinney, S. A. & Ha, T. Nonblinking and long-lasting single-molecule fluorescence imaging. *Nat. Methods* **3**, 891–893 (2006).
11. Schäfer, P., van de Linde, S., Lehmann, J., Sauer, M. & Doose, S. Methylene blue- and thiol-based oxygen depletion for super-resolutionimaging. *Anal. Chem.* **85**, 3393–3400 (2013).

12. Aitken, C. E., Marshall, R. A. & Puglisi, J. D. An oxygen dcavenging dystem for improvement of dye stability in single-molecule fluorescence experiments. *Biophys. J.* **94**, 1826–1835 (2008).
13. Zheng, Q. & Lavis, L. D. Development of photostable fluorophores for molecular imaging. *Curr. Opin. Chem. Biol.* **39**, 32–38 (2017).
14. Zheng, Q. et al. Ultra-stable organic fluorophores for single-molecule research. *Chem. Soc. Rev.* **43**, 1044–1056 (2014).
15. Zheng, Q. et al. On the Mechanisms of cyanine fluorophore photostabilization. *J. Phys. Chem. Lett.* **3**, 2200–2203 (2012).
16. Heilemann, M., vandeLinde, S., Mukherjee, A. & Sauer, M. Super-resolution imaging with small organic fluorophores. *Angew. Chem. Int. Ed.* **48**, 6903–6908 (2009).
17. Wang, Y., Fruhwirth, G., Cai, E., Ng, T. & Selvin, P. R. 3D Super-resolution imaging with blinking quantum dots. *Nano Lett.* **13**, 5233–5241 (2013).
18. Zrazhevskiy, P. & Gao, X. Quantum dot imaging platform for single-cell molecular profiling. *Nat. Commun.* **4**, 1619(2013).
19. Liu, Q. et al. Single upconversion nanoparticle imaging at sub-10 W cm−2 irradiance. *Nat. Photon.* **12**, 548–553 (2018).
20. Liu, Y. et al. Amplified stimulated emission in upconversion nanoparticles for super-resolution nanoscopy. *Nature* **543**, 229–233 (2017).
21. Zhan, Q. et al. Achieving high-efficiency emission depletion nanoscopy by employing cross relaxation in upconversion nanoparticles. *Nat. Commun.* **8**, 1058 (2017).
22. Jin, D. et al. Nanoparticles for super-resolution microscopy and single-molecule tracking. *Nat. Methods* **15**, 415–423 (2018).
23. Ao, Y. et al. An upconversion nanoparticle enables near infrared-optogenetic manipulation of the caenorhabditis elegans motor circuit. *ACS Nano.* **13**, 3373–3386 (2019).
24. Zeng, X. et al. Visualization of intra-neuronal motor protein transport through upconversion microscopy. *Angew. Chem. Int. Ed.* **58**, 9262–9268 (2019).
25. Dong, H. et al. Lanthanide nanoparticles: from design toward bioimaging and therapy. *Chem. Rev.* **115**, 10725–10815 (2015).
26. Zhu, X., Su, Q., Feng, W. & Li, F. Anti-Stokes shift luminescent materials for bio-applications. *Chem. Soc. Rev.* **46**, 1025–1039 (2017).
27. Chen, G., Qiu, H., Prasad, P. N. & Chen, X. Upconversion nanoparticles: design, nanochemistry, and applications in theranostics. *Chem. Rev.* **114**, 5161–5214 (2014).
28. Zheng, W. et al. Lanthanide-doped upconversion nano-bioprobes: electronic structures, optical properties, and biodetection. *Chem. Soc. Rev.* **44**, 1379–1415 (2015).
29. Peng, C. S. et al. Nanometer-resolution tracking of single cargo reveals dynein motor mechanisms. *Nat. Chem. Biol.* **21**, 648–656 (2024).
30. Zhang, Y. et al. Enhancement of single upconversion nanoparticle imaging by topologically segregated core-shell structure with inward energy migration. *Nat. Commum.* **13**, 5927 (2022).
31. Dukhno, O. et al. Targeted single particle tracking with upconverting nanoparticles. *ACS Appl. Mater. Interfaces* **16**, 11217–11227 (2024).
32. Wang, F., Wang, J. & Liu, X. Direct evidence of a surface quenching effect on size-dependent luminescence of upconversion nanoparticles. *Angew. Chem. Int. Ed.* **49**, 7456–7460 (2010).
33. Lei, L. et al. Amplifying upconversion by engineering interfacial density of state in sub-10 nm colloidal core/shell fluoride nanoparticles. *Nano Lett.* **21**, 10222–10229 (2021).
34. Xu, H. et al. Anomalous upconversion amplification induced by surface reconstruction in lanthanide sublattices. *Nat. Photon.* **15**, 732–737 (2021).
35. Gargas, D. J. et al. Engineering bright sub-10-nm upconverting nanocrystals for single-molecule imaging. *Nat. Nanotechnol.* **9**, 300–305 (2014).
36. Teitelboim, A. et al. energy transfer networks within upconverting nanoparticles are complex systems with collective, robust, and history-dependent dynamics. *J. Phys. Chem. C.* **123**, 2678–2689 (2019).
37. Li, Z. & Zhang, Y. An efficient and user-friendly method for the synthesis of hexagonal-phase NaYF(4):Yb, Er/Tm nanocrystals with controllable shape and upconversion fluorescence. *Nanotechnology* **19**, 345606 (2008).
38. Xia, X. et al. Accelerating the design of multishell upconverting nanoparticles through Bayesian optimization. *Nano Lett.* **23**, 11129–11136 (2023).
39. Wang, X. et al. Enhancing energy migration upconversion through a migratory interlayer in the core-shell-shell nanostructure towards latent fingerprinting. *Nanoscale* **12**, 18807–18814 (2020).
40. Kuhn, T., Hettich, J., Davtyan, R. & Gebhardt, J. C. M. Single molecule tracking and analysis framework including theory-predicted parameter settings. *Sci. Rep.* **11**, 9465 (2021).
41. Zanetti-Domingues, L. C. et al. The architecture of EGFR's basal complexes reveals autoinhibition mechanisms in dimers and oligomers. *Nat. Commun.* **9**, 4325 (2018).
42. Quan, T., Zeng, S. & Huang, Z. Localization capability and limitation of electron-multiplying charge-coupled, scientific complementary metal-oxide semiconductor, and charge-coupled devices for super-resolution imaging. *J. Biomed. Opt.* **15**, 066005 (2010).
43. Keersmaecker, H. D. et al. EGF receptor dynamics in EGF-responding cells revealed by functional imaging during single particle tracking. *Biophys. Rev. Lett.* **8**, 229–242 (2013).
44. Ling, H. et al. Effect of surface modification on the luminescence of individual upconversion nanoparticles. *Small* **20**, 2309035 (2024).
45. Sivonxay, E. et al. Inverse design of complex nanoparticle heterostructures via deep learning on heterogeneous graphs. ChemRxiv. https://doi.org/10.26434/chemrxiv-2024-1dw4q-v2 (2025).
46. Zichi, L. et al. RNMC: kinetic Monte Carlo implementations for complex reaction networks. *J. Open Sour. Softw.* **9**, 7244 (2024).
47. Thompson, R. E., Larson, D. R. & Webb, W. W. Precise nanometer localization analysis for individual fluorescent probes. *Biophys. J.* **82**, 2775–2783 (2002).

Acknowledgements

The authors thank Dr. Steven Chu (Stanford University) for his insightful discussions and valuable suggestions. The authors thank Dr. Eric Sivonxay for support simulating lifetimes. This work was financially supported by the National Key Research and Development Program of China (Grant No.2022YFB3503700 to Q.L.) and the National Natural Science Foundation of China (Grant No.22074021 to Q.L.; No. 22174025 to Y.Z.; and No. 21937003 to F.L.). Simulations were conducted at the Molecular Foundry using the National Energy Research Scientific Computing Center (NERSC, award BES-ERCAP0023292) and Lawrencium computational cluster resource at Lawrence Berkeley National Laboratory and were supported by the Office of Science, Office of Basic Energy Sciences, of the U.S. Department of Energy (DOE, No. DE- AC02-05CH11231, to E.C.).

Author contributions

Q.L., F.L., E. C., and Y.Z. supervised this project. X.Q. and H.L. was responsible for the design, synthesis, and characterization of upconversion nanoparticles. D.G. significantly contributed to the single-particle measurement and subsequent data analysis. X.X. and E.C. carried out computational investigations. J.H. participated in upconversion nanoparticles synthesis and characterization. The manuscript preparation involved Q.L., F.L., E. C., Y.Z., X.Q., D.G, and X.X., and all authors discussed and commented on the manuscript.

Competing interests

The authors declare no competing interests.

Additional information

Supplementary information The online version contains supplementary material available at https://doi.org/10.1038/s41467-025-64180-w.

Correspondence and requests for materials should be addressed to Yunxiang Zhang, Emory Chan, Fuyou Li or Qian Liu.

Peer review information *Nature Communications* thanks Ute Resch-Genger, and the other, anonymous, reviewer(s) for their contribution to the peer review of this work. A peer review file is available.

Reprints and permissions information is available at http://www.nature.com/reprints

Publisher's note Springer Nature remains neutral with regard to jurisdictional claims in published maps and institutional affiliations.

Open Access This article is licensed under a Creative Commons Attribution-NonCommercial-NoDerivatives 4.0 International License, which permits any non-commercial use, sharing, distribution and reproduction in any medium or format, as long as you give appropriate credit to the original author(s) and the source, provide a link to the Creative Commons licence, and indicate if you modified the licensed material. You do not have permission under this licence to share adapted material derived from this article or parts of it. The images or other third party material in this article are included in the article's Creative Commons licence, unless indicated otherwise in a credit line to the material. If material is not included in the article's Creative Commons licence and your intended use is not permitted by statutory regulation or exceeds the permitted use, you will need to obtain permission directly from the copyright holder. To view a copy of this licence, visit http://creativecommons.org/licenses/by-nc-nd/4.0/.

© The Author(s) 2025